FINITE-DIFFERENCE SIMULATION OF LINEAR PLATE VIBRATION WITH DYNAMIC DISTRIBUTED CONTACT

Maarten VAN WALSTIJN[1,2], **Abhiram BHANUPRAKASH**[1,2], and **Paul STAPLETON**[1,3]

[1] *Sonic Arts Research Centre*, **Queen's University Belfast**, UK
[2] *School of Electronics, Electrical Engineering and Computer Science*, **Queen's University Belfast**, UK
[3] *School of Arts, English, and Languages*, **Queen's University Belfast**, UK

ABSTRACT

The potential of physics-based synthesis algorithms for developing computer-based musical instruments relies on the inclusion of articulatory elements that enable physically plausible and musically meaningful interactions. In this paper, non-excitational interaction with a rectangular vibrating plate is modelled through time variation in distributed contact parameters. For numerical simulation a finite difference approach is taken, enabling efficient modelling of local interactions. Comparison between the continuous- and discrete-domain system power balances confirms conditional stability and a match in the source terms due to parameter time-variance. The methodology is exemplified with a few case studies, and its potential for application in the design of a virtual-acoustic plate-based musical instrument is discussed.

1. INTRODUCTION

Music performed with mechano-acoustic instruments is often articulated through physical contact, either directly between the musician and a resonating element or via an extension (e.g. a mallet, bow, or slide). Such embodied interaction generally serves two kinds of purposes. The first is to inject energy into the instrument's vibrating parts, such as plucking a string or striking a membrane. The second is to alter the vibrating properties of the instrument, for example holding down a string against a fretboard to achieve a specific pitch. Some forms of contact serve both purposes simultaneously, e.g. guitar tapping [1].

In the case of 2-D vibrating systems, such as membranes and plates featuring in percussion instruments, contact for the second purpose is often of a distributed nature, and generally involves *damping*, *clamping*, and *mass-loading*. For any specific form of contact, typically one of those phenomena dominates. For example, Figure 2(a) displays a common way to damp the sound of a vibrating cymbal, in which the hand's strong damping is accompanied by small additional stiffness (which can be considered as clamping) and mass-loading. The spectrogram in Figure 2(d) of a recorded cymbal strike with hand damping applied at around $t = 1.2$s shows how the partials may not be damped to the same extent, and also shows slight lowering of some of the resonance frequencies. Figure 2(b) shows a partially clamped vibraphone bar, introducing spring-like distributed restoring forces over the clamped region, and altering the resonant characteristics. As can be seen in the spectra shown in Figure 2(e), the specific resonance alterations depend on where the system is clamped. Somewhat similar to placing a capo on the guitar neck, this form of contact is conducted more on the level of design and reconfiguration than performatory action. Figure 2(c) shows the partial submersion of a small round gong in water, effectively introducing strong mass-loading on the submerged region, which lowers the resonance frequencies. Modulating the plate's resonance frequencies by dynamically changing the amount of submerged plate surface is an established performance practice with gongs and tam-tams (see, e.g. [2]). Figure 2(f) shows the spectrogram of a gong strike followed by gradually lifting the gong upwards and then back downwards, thus effecting a temporary decrease in submerged surface area.

Copyright: © 2021 the Authors. This is an open-access article distributed under the terms of the Creative Commons Attribution 4.0 International License, which permits unrestricted use, distribution, and reproduction in any medium, provided the original author and source are credited.

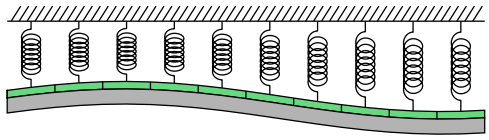

Figure 1. Schematic representation of the locally reacting contact layer. The grey object represents the plate, and the green elements represent additional surface density. The springs represent additional stiffness and damping per unit area.

From a music articulation perspective, dynamic contact is of particular interest. The three aforementioned phenomena are therefore considered here as time-varying.

This paper focuses on the simulation of such time-varying, non-excitational distributed contact, with a view to facilitate physically plausible contact with intuitive parameter control in physics-based sound synthesis, using a rectangular plate model with free edges as a testbed 2-D resonator. The approach is to model the contact in terms of additional damping, stiffness, and mass-loading terms (see Figure 1), in effect adding what is known in room acoustics as a locally-reacting layer. Similar to earlier work on modelling string excitation [3, 4], dynamic contact is emulated via time variation of the local contact parameters. For example, initiating contact of a hand with

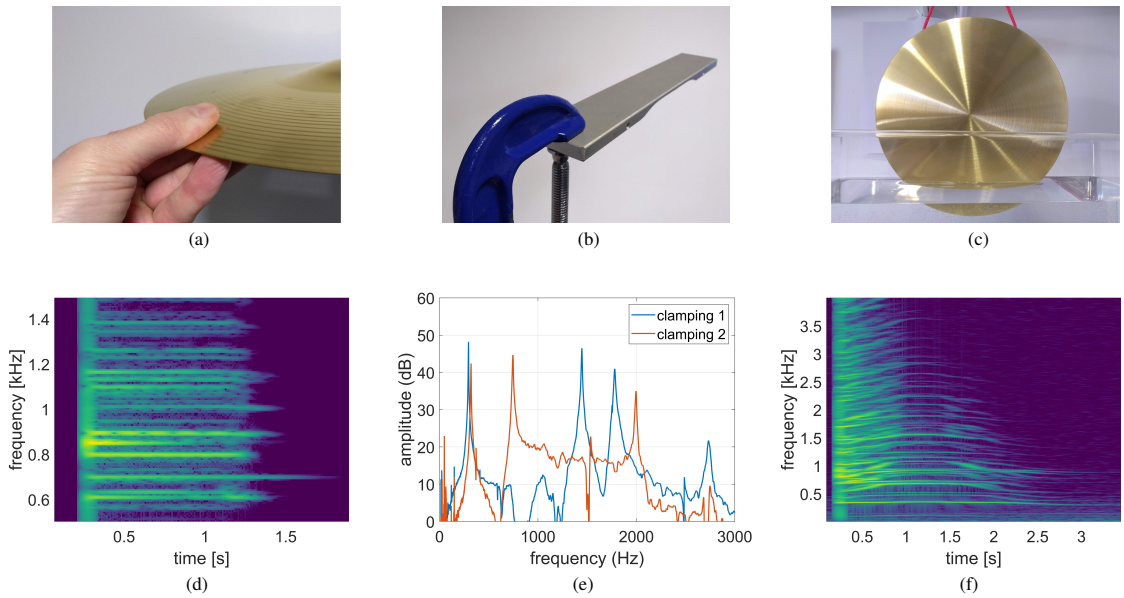

Figure 2. Examples of distributed contact in 2-D musical resonators: (a) regional damping of a cymbal via local hand contact, (b) regional clamping of a vibraphone bar, (c) regional mass loading of a round gong by submerging it partially in water, (d) spectrogram of a cymbal strike with hand damping at $t = 1.2$ s, (e) amplitude spectra of a struck vibraphone bar clamped at two different positions, (f) spectrogram of a gong with time-varying water submersion.

the plate is modelled by ramping up from zero the spring stiffness and damping per unit area as well as the surface density. For static values of the contact parameters the model is grounded in Newtonian physics, but the specification of how the parameters vary to emulate dynamic contact is, due to the simplifications involved, more phenomenological. It would be more physically correct to model the motion of the hand or other external object separately, allowing also to simulate collisions, such as recently reported in the context of slide-string articulation in [5]. The reasons for not taking a more complex approach are (a) collisions have a limited role in most practical examples of non-excitational contact (except for sympathetic vibrations, which can be modelled separately), (b) it would require updating a large set of additional mass positions, adding significant computational burden, and (c) in a real-time scenario, the distance between the object and the 2-D resonator would have to be sensed across the spatial coordinates, which is a challenge in its own right. For the simpler model chosen, only a pressure map needs to be sensed, which can be done with available sensing devices, such as the Sensel Morph [1]; the local contact parameters may then be specified as an implicit function of the local control pressure.

Regarding the modelling of plate vibrations, i.e. the system without contact terms, the equations of motion given in Section 2 and their discretisation and associated energy analysis presented in Section 3 are equivalent to those presented in earlier work on plate modelling [6, 7]. The novel aspect in these sections revolves around the introduction of the time-varying contact terms and their discretisation.

[1] https://sensel.com/

2. PLATE MODEL WITH CONTACT

Let $\partial_x u$ and $d_x u$ denote the partial and total derivative of u with respect to x, respectively.

2.1 System Equations

Consider transversal vibrations of a thin plate with damping and distributed contact terms:

$$\rho h \partial_t^2 u = -D\Delta^2 u + 2\rho h \left[\sigma_2 \Delta - \sigma_0\right] \partial_t u + \psi F_\mathrm{e} \underbrace{-\partial_t(\bar{\lambda}\partial_t u) - \bar{k}u - 2\rho h \bar{\sigma} \partial_t u}_{\text{contact}}, \quad (1)$$

where $u = u(x, y, t)$ denotes transversal displacement, ρ is mass density, and σ_0 and σ_2 are damping constants. The parameter $D = \frac{1}{12}Eh^3/(1-\nu^2)$ can be considered as characterising the plate stiffness, where E is the Young's modulus, h is the plate thickness, and ν is the Poisson's ratio. The first term on the right-hand side of (1) can be written

$$\begin{aligned} -D\Delta^2 u &= -D\left(\partial_x^4 + \partial_y^4 + 2\partial_x^2\partial_y^2\right) u, \\ &= \partial_x^2 m_x + \partial_y^2 m_y + 2\partial_x\partial_y m_{xy}, \end{aligned} \quad (2)$$

where the plate bending moments

$$m_x = -D\left(\partial_x^2 u + \nu\partial_y^2 u\right), \quad (3)$$

$$m_y = -D\left(\partial_y^2 u + \nu\partial_x^2 u\right), \quad (4)$$

$$m_{xy} = -D\left(1-\nu\right)\partial_x\partial_y u, \quad (5)$$

are introduced due to their usefulness in defining boundary conditions and in performing energy analysis. The term $\psi = \psi(x, y, t) = \delta_D(x - x_\mathrm{e}(t), y - y_\mathrm{e}(t))$ defines the position of the driving force $F_\mathrm{e} = F_\mathrm{e}(t)$.

The lower line in (1) contains three time-varying terms due to distributed contact, in accordance with Figure 1. The contact surface density $\bar{\lambda} = \bar{\lambda}(x, y, t)$, stiffness $\bar{k} = \bar{k}(x, y, t)$ and damping $\bar{\sigma} = \bar{\sigma}(x, y, t)$ are each modelled here as being dependent on a non-dimensional distributed control pressure map $\bar{p} = \bar{p}(x, y, t)$:

$$\bar{\lambda} = a_\lambda \bar{p}, \quad \bar{k} = a_k \bar{p}, \quad \bar{\sigma} = a_\sigma \bar{p}(1 + \bar{g}) + \sigma_0 \bar{g}, \tag{6}$$

where $\bar{g} = \bar{\lambda}/(\rho h)$ and $a_i \geq 0$, $i \in \{\lambda, k, \sigma\}$ can be tuned to suit specific interaction design purposes, and with $0 \leq \bar{p} \leq 1$. The control pressure is a map that - for real-time application - could be sensed with a force-sensitive electronic pad, such as the Sensel Morph. Grouping common terms, one can re-write (1) as

$$\partial_t \left[\left(\rho h + \bar{\lambda} \right) \partial_t u \right] = - \left[D\Delta^2 + \bar{k} \right] u + \psi F_\mathrm{e} + 2\rho h \left[\sigma_2 \Delta - (\bar{\sigma} + \sigma_0) \right] \partial_t u. \tag{7}$$

Hence the effective frequency-independent damping is

$$\sigma_{0,\mathrm{eff}} = \frac{2\rho h \left(\bar{\sigma} + \sigma_0 \right)}{2 \left(\rho h + \bar{\lambda} \right)} \overset{(6)}{=} \sigma_0 + a_\sigma \bar{p}, \tag{8}$$

which shows how the specific form for $\bar{\sigma}$ in (6) facilitates direct control of the effective additional local damping. Eq. (7) also brings to light how practical ranges for each of the contact parameters are relative to the 'corresponding' plate parameters.

2.2 Boundary Conditions

Free boundary conditions are imposed, mainly to enable a natural way of damping by grabbing the edge of the plate (like in cymbals, see Figure 2a). For a rectangular plate of size $L_x \times L_y$, at the edges we have [8]

$$x = 0, L_x : \quad m_x = 0, \quad \partial_x m_x + 2\partial_y m_{xy} = 0, \tag{9}$$
$$y = 0, L_y : \quad m_y = 0, \quad \partial_y m_y + 2\partial_x m_{xy} = 0, \tag{10}$$

Through substitution this can be written as

$$x{=}0, L_x: \quad \partial_x^2 u + \nu \partial_y^2 u = 0, \quad \partial_x^3 u + (2-\nu)\partial_x \partial_y^2 u = 0, \tag{11}$$
$$y{=}0, L_y: \quad \partial_y^2 u + \nu \partial_x^2 u = 0, \quad \partial_y^3 u + (2-\nu)\partial_y \partial_x^2 u = 0. \tag{12}$$

An additional condition is required at corners:

$$m_{xy} = 0, \implies \partial_x \partial_y u = 0. \tag{13}$$

2.3 Energy Analysis

Given the functions $f(x, y, t)$ and $g(x, y, t)$, let's define the plate domain

$$\mathcal{P} = \{(x, y) \in \mathbb{R} \,|\, 0 \leq x \leq L_x, 0 \leq y \leq L_y\} \tag{14}$$

and the associated inner product and norm

$$\langle f, g \rangle_\mathcal{P} = \int_{y=0}^{L_y} \int_{x=0}^{L_x} f(x, y, t)\, g(x, y, t)\, dx dy, \tag{15}$$
$$\|f\|_\mathcal{P} = \sqrt{\langle f, f \rangle_\mathcal{P}}, \tag{16}$$

which will allow compact notation of energy terms. Multiplying (1) with $\partial_t u$ and integrating over the plate domain $\mathcal{P}$, one obtains the power balance

$$d_t \left(H_\mathrm{p} + H_\mathrm{c} \right) = P_\mathrm{e} + P_\mathrm{c} - Q_\mathrm{p} - Q_\mathrm{c}, \tag{17}$$

with the (non-negative) energy components

$$H_\mathrm{p} = \frac{1}{D(1-\nu^2)} \left[\tfrac{1}{2} \|m_x\|_\mathcal{P}^2 + \tfrac{1}{2} \|m_y\|_\mathcal{P}^2 - \nu \langle m_x, m_y \rangle_\mathcal{P} \right] + \tfrac{1}{2} \rho h \|\partial_t u\|_\mathcal{P}^2 + \frac{1}{D(1-\nu)} \|m_{xy}\|_\mathcal{P}^2, \tag{18}$$
$$H_\mathrm{c} = \tfrac{1}{2} \langle \bar{k} u, u \rangle_\mathcal{P} + \tfrac{1}{2} \langle \bar{\lambda}\, \partial_t u, \partial_t u \rangle_\mathcal{P}. \tag{19}$$

The power input terms (of indeterminate sign) are

$$P_\mathrm{e} = F_\mathrm{e} \langle \psi, \partial_t u \rangle_\mathcal{P}, \tag{20}$$
$$P_\mathrm{c} = \tfrac{1}{2} \langle u\, \partial_t \bar{k}, u \rangle_\mathcal{P} - \tfrac{1}{2} \langle \partial_t u\, \partial_t \bar{\lambda}, \partial_t u \rangle_\mathcal{P}. \tag{21}$$

and the (non-negative) damping terms are

$$Q_\mathrm{p} = 2\rho h \left(\sigma_0 \|\partial_t u\|_\mathcal{P}^2 + \sigma_2 \|\partial_t \nabla u\|_\mathcal{P}^2 \right), \tag{22}$$
$$Q_\mathrm{c} = 2\rho h \langle \bar{\sigma}\, \partial_t u, \partial_t u \rangle_\mathcal{P}. \tag{23}$$

In the above, the subscripts 'p', 'c', and 'e' indicate 'plate', 'contact', and 'excitation', respectively. As explained in [7], additional boundary terms in (17) obtained initially after integration by parts vanish for the boundary conditions in (9), (10), and (13).

3. NUMERICAL FORMULATION

3.1 Discretisation Operators

Employing the usual spatio-temporal gridding notation $u_{l,m}^n$ to denote u at time $t = n\Delta_t$ and position $x = l\Delta_x$, $y = m\Delta_x$, the following shift operators are defined:

$$\epsilon_{t+} u_{l,m}^n = u_{l,m}^{n+\frac{1}{2}}, \qquad \epsilon_{t-} u_{l,m}^n = u_{l,m}^{n-\frac{1}{2}}. \tag{24}$$

Elemental temporal difference and averaging operators can then be constructed as

$$\delta_t = \frac{\epsilon_{t+} - \epsilon_{t-}}{\Delta_t}, \qquad \mu_t = \frac{\epsilon_{t+} + \epsilon_{t-}}{2}, \tag{25}$$
$$\delta_{t+} = \frac{\epsilon_{t+}^2 - 1}{\Delta_t}, \qquad \mu_{t+} = \frac{\epsilon_{t+}^2 + 1}{2}, \tag{26}$$
$$\delta_{t-} = \frac{1 - \epsilon_{t-}^2}{\Delta_t}, \qquad \mu_{t-} = \frac{1 + \epsilon_{t-}^2}{2}. \tag{27}$$

Various finite-difference approximations can be achieved by directly applying or combining these elemental operators, e.g.

$$\delta_t^2 u_{l,m}^n = \frac{u_{l,m}^{n+1} - 2u_{l,m}^n + u_{l,m}^{n-1}}{\Delta_t^2} \approx (\partial_t^2 u)^*, \tag{28}$$
$$\delta_{t\cdot} u_{l,m}^n := \delta_t \mu_t u_{l,m}^n = \frac{u_{l,m}^{n+1} - u_{l,m}^{n-1}}{2\Delta_t} \approx (\partial_t u)^*, \tag{29}$$
$$\mu_t^2 u_{l,m}^n = \frac{u_{l,m}^{n+1} + 2u_{l,m}^n + u_{l,m}^{n-1}}{4} \approx u^*, \tag{30}$$

where the asterisk denotes that the relevant quantity is evaluated at time $n\Delta_t$ and position $(l\Delta_x, m\Delta_x)$. Spatial operators can be defined analogously, by replacing t with x or y in the above, and using $\Delta_y = \Delta_x$ for convenient analysis and implementation [6]. A discrete Laplacian and biharmonic operator can be constructed as

$$\tilde{\Delta} = \delta_x^2 + \delta_y^2, \tag{31}$$

$$\tilde{\Delta}^2 = \delta_x^4 + 2\delta_x^2\delta_y^2 + \delta_y^4. \tag{32}$$

3.2 Product Identities

The following product identities hold for any two time series $f = f^n$ and $g = g^n$:

$$\mu_t\left(\mu_t f \cdot \mu_t g\right) \cdot \delta_{t\cdot} g = \tfrac{1}{2}\delta_t\left[\mu_t f \cdot (\mu_t g)^2\right] - \delta_{t\cdot} f \cdot \mu_{t+} g \cdot \mu_{t-} g, \tag{33}$$

$$\delta_t\left(\mu_t f\, \delta_t g\right) \cdot \delta_{t\cdot} g = \tfrac{1}{2}\delta_t\left[\mu_t f \cdot (\delta_t g)^2\right] + \delta_{t\cdot} f \cdot \delta_{t+} g \cdot \delta_{t-} g, \tag{34}$$

which is easily proven by direct evaluation of the terms to which discretisation operators are applied. These identities are useful in energy analysis regarding the terms with time-varying parameters. For the time-invariant terms, here relating to plate vibrations, use can be made of a handful of identities involving inner products (see, e.g. [6, 7]).

3.3 Numerical Scheme

The fully explicit numerical scheme employed here results from applying discretisation operators to (7) as follows:

$$\begin{aligned}\delta_t\left[\left(\rho h + \mu_t \bar{\lambda}_{l,m}^n\right)\delta_t u_{l,m}^n\right] = &-D\tilde{\Delta}^2 u_{l,m}^n + \psi_{l,m}^n F_{\mathrm{e}}^n \\ &- \mu_t\left(\mu_t \bar{k}_{l,m}^n\, \mu_t u_{l,m}^n\right) \\ &- 2\rho h\left[\bar{\sigma}_{l,m}^n + \sigma_0\right]\delta_{t\cdot} u_{l,m}^n \\ &+ 2\rho h\sigma_2 \tilde{\Delta}\delta_{t-} u_{l,m}^n,\end{aligned} \tag{35}$$

where $\psi_{l,m}^n$ is a discrete-domain version of the distribution function $\psi(x, y, t)$ obtained through bilinear de-interpolation. Dropping the indexes in the notation, e.g. $u = u_{l,m}^n$, one may write the first term on the right-hand side in terms of the discretised moments:

$$-D\tilde{\Delta}^2 u = \delta_x^2 m_x + \delta_y^2 m_y + 2\delta_{x-}\delta_{y-} m_{xy}, \tag{36}$$

where

$$m_x = -D\left(\delta_x^2 u + \nu\delta_y^2 u\right), \tag{37}$$

$$m_y = -D\left(\delta_y^2 u + \nu\delta_x^2 u\right), \tag{38}$$

$$m_{xy} = -D\left(1-\nu\right)\delta_{x+}\delta_{y+} u, \tag{39}$$

with $m_{xy} = m_{xy,l+\frac{1}{2},m+\frac{1}{2}}^n$. By substitution, we can recover the biharmonic operator in the form of (32).

3.4 Boundary Conditions

Using a non-centered approach for the boundaries, at the left and bottom edge one may specify [7]:

$$x{=}0: \quad m_x{=}0, \quad \delta_{x-} m_x + 2e_{x-}\delta_{y-} m_{xy} = 0, \tag{40}$$

$$y{=}0: \quad m_y{=}0, \quad \delta_{y-} m_y + 2e_{y-}\delta_{x-} m_{xy} = 0. \tag{41}$$

Through substitution we obtain:

$$x{=}0: \quad \delta_x^2 u + \nu\delta_y^2 u = 0, \quad \delta_{x-}\left[\delta_x^2 u + (2-\nu)\delta_y^2\right] u = 0, \tag{42}$$

$$y{=}0: \quad \delta_y^2 u + \nu\delta_x^2 u = 0, \quad \delta_{y-}\left[\delta_y^2 u + (2-\nu)\delta_x^2\right] u = 0, \tag{43}$$

which is analogous to (11,12). For the corner at $x = 0, y = 0$, a suitable numerical condition is

$$e_{x-} e_{y-} m_{xy} = 0, \implies \delta_{x-}\delta_{y-} u_{l,m}^n = 0. \tag{44}$$

Appropriately symmetric versions of the above conditions are applied to the other edges and corners.

3.5 Energy Analysis

For non-centered boundaries, the numerical inner product takes the form [6, 7]

$$\langle f, g\rangle_{\mathcal{P}} = \sum_{l=0}^{M_x}\sum_{m=0}^{M_y} f_{l,m}^n\, g_{l,m}^n\, \Delta_x^2. \tag{45}$$

where M_x and M_y define the grid size. After multiplying (35) with $\delta_{t\cdot} u$ and performing summation by parts, one obtains the power balance

$$\delta_t\left(H_{\mathrm{p}}^n + H_{\mathrm{c}}^n\right) = P_{\mathrm{e}}^n + P_{\mathrm{c}}^n - Q_{\mathrm{p}}^n - Q_{\mathrm{c}}^n, \tag{46}$$

where, making use of the product identities presented in Section 3.2, the energy components and power input terms can be specified as

$$\begin{aligned}H_{\mathrm{p}}^{n+\frac{1}{2}} = &\tfrac{1}{2}\rho h\|\delta_{t+} u\|_{\mathcal{P}} + \frac{1}{D(1-\nu)}\langle m_{xy}, e_{t+} m_{xy}\rangle_{\mathcal{P}} \\ &- \tfrac{1}{2}\rho h\sigma_2\Delta_t\left(\|\delta_{t+}\delta_{x+} u\|_{\mathcal{P}}^2 + \|\delta_{t+}\delta_{y+} u\|_{\mathcal{P}}^2\right) \\ &+ \frac{1}{D(1-\nu^2)}\Big[\tfrac{1}{2}\langle m_x, e_{t+} m_x\rangle_{\mathcal{P}} \\ &+ \tfrac{1}{2}\langle m_y, e_{t+} m_y\rangle_{\mathcal{P}} - \tfrac{1}{2}\nu\langle m_x, e_{t+} m_y\rangle_{\mathcal{P}} \\ &- \tfrac{1}{2}\nu\langle e_{t+} m_x, m_y\rangle_{\mathcal{P}}\Big],\end{aligned} \tag{47}$$

$$\begin{aligned}H_{\mathrm{c}}^{n+\frac{1}{2}} = &\tfrac{1}{2}\langle\mu_{t+}\bar{k}\,\mu_{t+} u, \mu_{t+} u\rangle_{\mathcal{P}} \\ &+ \tfrac{1}{2}\langle\delta_{t+} u\,\mu_{t+}\bar{\lambda}, \delta_{t+} u\rangle_{\mathcal{P}},\end{aligned} \tag{48}$$

$$P_{\mathrm{e}}^n = F_{\mathrm{e}}^n\langle\psi, \delta_{t\cdot} u\rangle_{\mathcal{P}}, \tag{49}$$

$$P_{\mathrm{c}}^n = \tfrac{1}{2}\langle\mu_{t+} u\,\mu_{t-} u, \delta_{t\cdot}\bar{k}\rangle_{\mathcal{P}} - \tfrac{1}{2}\langle\delta_{t+} u\,\delta_{t-} u, \delta_{t\cdot}\bar{\lambda}\rangle_{\mathcal{P}}. \tag{50}$$

The damping terms are

$$\begin{aligned}Q_{\mathrm{p}}^n = &2\rho h\Big[\sigma_0\|\delta_{t\cdot} u\|_{\mathcal{P}}^2 \\ &+ \sigma_2\left(\|\delta_{t\cdot}\delta_{x-} u\|_{\mathcal{P}}^2 + \|\delta_{t\cdot}\delta_{y-} u\|_{\mathcal{P}}^2\right)\Big],\end{aligned} \tag{51}$$

$$Q_{\mathrm{c}}^n = 2\rho h\langle\bar{\sigma}\,\delta_{t\cdot} u, \delta_{t\cdot} u\rangle_{\mathcal{P}}. \tag{52}$$

As before with the continuous-domain power balance, additional boundary terms in (46) obtained initially after summation by parts vanish for the boundary conditions in (40), (41), and (44). The scheme can thus be said to be stable under the condition that the numerical system energy $H^{n+\frac{1}{2}} = H_{\mathrm{p}}^{n+\frac{1}{2}} + H_{\mathrm{c}}^{n+\frac{1}{2}}$ remains non-negative. Given that

$H_{\mathrm{c}}^{n+\frac{1}{2}} \geq 0$ without further conditions, this requires non-negativity of $H_{\mathrm{p}}^{n+\frac{1}{2}}$, which can be shown to hold if

$$\Delta_x \geq \Delta_x^{\min} = \sqrt{4\Delta_t \left(\sigma_2 + \sqrt{\sigma_2^2 + D/(\rho h)}\right)}. \quad (53)$$

In implementatons, this condition is met by setting $\Delta_x = \Delta_x^{\min}$ and adjusting the plate dimensions to fit to the grid:

$$L_x = \underbrace{\lfloor L_x'/\Delta_x \rfloor}_{M_x} \Delta_x, \quad L_y = \underbrace{\lfloor L_y'/\Delta_x \rfloor}_{M_y} \Delta_x, \quad (54)$$

where L_x' and L_y' are the initial target dimensions. Comparison of the above equations with those of section 2.3 reveals that, provided that the stability condition is satisfied, the numerical system mirrors the energy behaviour of its underlying continuous-domain counterpart, in that (a) the system is strictly dissipative in the absence of external forces and time-variation in the contact parameters, and (b) variation in $\bar{\lambda}$ or $\bar{k}$ results in articulatory power sources of matching form, i.e. (50) takes the form of a direct discretisation of (21).

3.6 Update Equation

For the scheme in (35) one can derive the general update equation:

$$\begin{aligned}\Big[c_0 + \bar{\zeta}_{l,m}^n + \bar{\kappa}_{l,m}^{n+\frac{1}{2}} + \bar{\gamma}_{l,m}^{n+\frac{1}{2}}\Big] u_{l,m}^{n+1} = \\ \Big[c_3 - (\bar{\kappa}_{l,m}^{n+\frac{1}{2}} + \bar{\kappa}_{l,m}^{n-\frac{1}{2}}) + (\bar{\gamma}_{l,m}^{n+\frac{1}{2}} + \bar{\gamma}_{l,m}^{n-\frac{1}{2}})\Big] u_{l,m}^n \\ + \Big[c_4 + \bar{\zeta}_{l,m}^n - \bar{\kappa}_{l,m}^{n-\frac{1}{2}} - \bar{\gamma}_{l,m}^{n-\frac{1}{2}}\Big] u_{l,m}^{n-1} \\ + c_2 v_{l,m}^n + c_5 v_{l,m}^{n-1} + c_1\Big[2s_{l,m}^n + w_{l,m}^n\Big] \\ + c_6\Big[\psi_{l,m}^n F_{\mathrm{e}}^n\Big]. \quad (55)\end{aligned}$$

where

$$v_{l,m}^n = u_{l+1,m}^n + u_{l-1,m}^n + u_{l,m+1}^n + u_{l,m-1}^n, \quad (56)$$

$$w_{l,m}^n = u_{l+2,m}^n + u_{l-2,m}^n + u_{l,m+2}^n + u_{l,m-2}^n, \quad (57)$$

$$s_{l,m}^n = u_{l+1,m+1}^n + u_{l-1,m+1}^n + u_{l+1,m-1}^n + u_{l-1,m-1}^n. \quad (58)$$

Note that for nodes on and near the boundary, ghost-nodes (nodes falling outside the domain) come into play in the expressions in (56), (57) and (58), and these need to be substituted for using the boundary conditions in (42), (43), and (44). The various coefficients in (55) are defined as

$$\bar{\kappa}_{l,m}^{n+\frac{1}{2}} = \tfrac{1}{4}\xi\mu_t \bar{k}_{l,m}^{n+\frac{1}{2}}, \qquad \bar{\gamma}_{l,m}^{n+\frac{1}{2}} = \mu_t \bar{g}_{l,m}^{n+\frac{1}{2}}, \quad (59)$$

$$c_0 = 1 + \zeta_0, \qquad c_1 = -K^2, \quad (60)$$

$$c_2 = 8K^2 + \zeta_2, \qquad c_3 = 2 - 20K^2 - 4\zeta_2, \quad (61)$$

$$c_4 = -1 + 4\zeta_2 + \zeta_0, \quad c_5 = -\zeta_2, \qquad c_6 = \xi, \quad (62)$$

with

$$K = \sqrt{\frac{D}{\rho h}\frac{\Delta_t}{\Delta_x^2}}, \quad \zeta_0 = \sigma_0 \Delta t, \qquad \zeta_2 = \frac{2\sigma_2 \Delta t}{\Delta_x^2},$$

$$\bar{\zeta}_{l,m}^n = \bar{\sigma}_{l,m}^n \Delta_t, \qquad \xi = \frac{\Delta_t^2}{\rho h}, \qquad \bar{g}_{l,m}^n = \frac{\bar{\lambda}_{l,m}^n}{\rho h}. \quad (63)$$

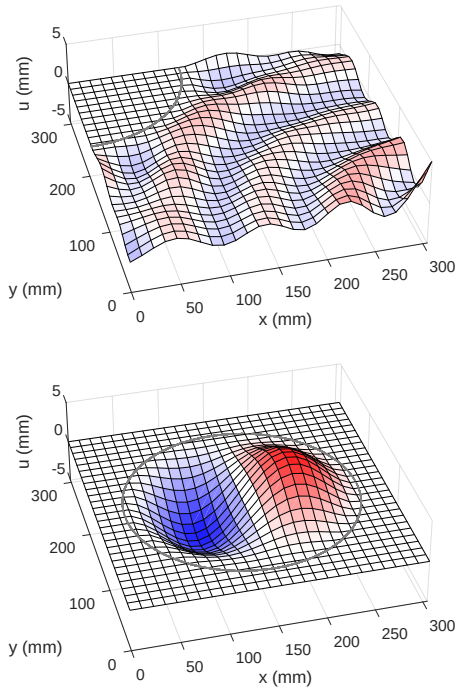

Figure 3. Examples of regional clamping of a square-shaped steel plate. Top: corner region clamp. Bottom: circular plate with clamped edges.

4. NUMERICAL EXPERIMENTS

In this section, the functionality of the model is demonstrated with a few examples. In all cases, the material parameters used are $E = 200$ GPa, $\rho = 8000$ kg/m^3 and $\nu = 0.3$, which are typical of steel. The simulations are run using $\Delta_t = 1/44100$ s. To help manage potential drift, a very small additional amount of clamping ($\bar{k} = 100$ N/m^3) is systematically applied across the plate.

4.1 Static Contact

4.1.1 Regional Clamping

Figure 3 shows snapshots of two simulations in which a specific region of a square plate was clamped by setting $\bar{k} = 10^{13}$ N/m^3 in that region. In the first experiment (see top plot in Figure 3), a small quarter-circular region at one of the corners was clamped, and the system was brought into vibration by driving the opposite corner with a sinusoid. For such a high $\bar{k}$ value, practically no oscillation can occur in the clamped region. Setting lower values facilitates softly clamped regions, which lead to different system resonances. In the second experiment (see bottom plot in Figure 3), the clamped region was chosen as lying outside a centrally-positioned circle, allowing the simulation of a clamped circular plate, albeit accepting approximations in terms of the domain shape due to the spatial discretisation. The system was driven off-center with the second lowest resonance frequency of the system, as such revealing the shape of its (1,1) normal mode.

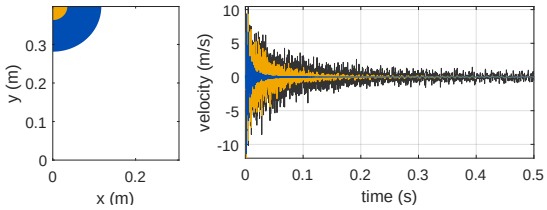

Figure 4. Contact damping ($\bar{\sigma} = 1000$ s^{-1}) over differently sized regions. The plate was excited at its lower right corner. Left: regions. Right: impulse responses. The dark grey curve is the impulse response with no contact damping applied. The blue and orange curves match the same-colour damping regions in the left-hand side plot.

4.1.2 *Regional Damping*

Similarly, one may apply a non-zero $\bar{\sigma}$ value to a region of the plate, in order to locally effect damping. Figure 4 compares the impulse response of a rectangular plate for two different damping regions with the impulse response of the same plate with no contact damping applied. The expected observation of stronger damping with larger contact area also gives an indication of the requirement of any contact damping having to be distributed in order to facilitate strong damping. In other words, there is little scope for modelling strong damping through a single contact point.

4.2 Dynamic Contact

For dynamic contact, the pressure map $\bar{p}^n_{l,m}$ is updated every sample by linearly interpolating between control-rate updates made every N_b samples, setting $N_\mathrm{b} = 256$. Sound examples are available on the companion webpage [2].

4.2.1 *Damping of a Single Pulse*

A square plate of side length $L_x = L_y = 0.1415$ m and thickness $h = 1.8$ mm is excited at coordinates $x_\mathrm{e} = 0.77L_x$, $y_\mathrm{e} = 0.5L_y$. A velocity output signal is picked up at $x_\mathrm{p} = 0.95L_x$, $y_\mathrm{p} = 0.11L_y$. The plate damping parameters were set as $\sigma_0 = 1$ s^{-1} and $\sigma_2 = 0.001$ m^2 s^{-1}. Contact damping is applied after 1.6 seconds over a circular area of radius 42.4 mm, with the circle centre positioned at $x = 0.1L_x$, $y = 0.5L_y$ (see the top plot in Figure 5). The damping is effected through linearly increasing the control pressure uniformly over the circular region, according to the profile shown in the middle plot of Figure 5. The contact-layer constants featured in equation (6) were set to $a_k = 10000$ N m^{-3}, $a_\sigma = 250$ s^{-1}, and $a_\lambda = 7.2$ kg m^{-2} in order to simulate hand-plate contact with somewhat exaggerated mass loading. The output spectrogram is shown in the bottom plot. Of particular interest is the small decrease in partial frequencies, which is due to the increase in surface density. In addition, it is noticable that some partials are damped more effectively than others, which is mainly due to the chosen region over which damping is applied. One can also observe a small amount of broadband power injected at $t = 1.6$ s, which corresponds to the term

[2] www.socasites.qub.ac.uk/mvanwalstijn/smc21b

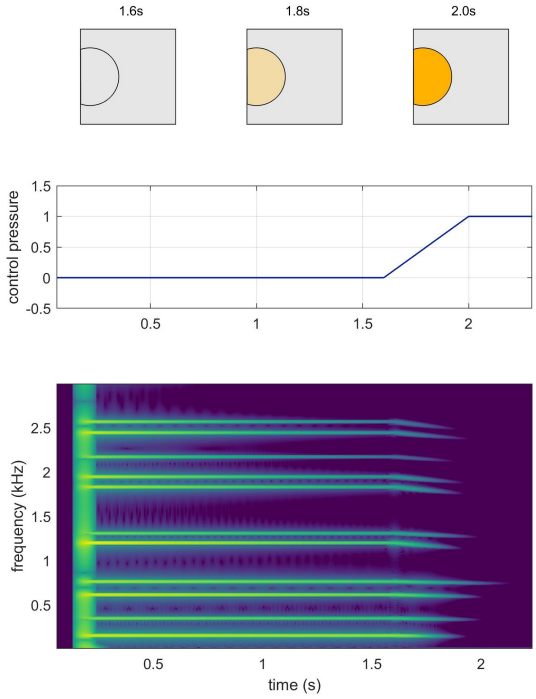

Figure 5. Pulse damping example. The top plot shows the region over which damping was increased according to the profile shown in the middle plot, while the bottom plot shows the output spectrogram.

P_c in the power balance equation in (46), and is due to the variation over time of the contact parameters.

4.2.2 *Linear Water Gong*

In this example, the plate geometrical parameters are set as $L_x = L_y = 0.2983$ m and $h = 2$ mm, and the damping parameters are $\sigma_0 = 1$ s^{-1} and $\sigma_2 = 0.0016$ m^2 s^{-1}. To emulate suspension of the plate, clamping is applied at the corner with coordinates $x = L_x, y = L_y$. The plate is partly submerged into water at the opposite plate corner ($x = 0, y = 0$), the water level reaching 30 percent of the diagonal between the two opposite corners. The plate is excited at $x_\mathrm{e} = 0.88L_x$, $y_\mathrm{e} = 0.87L_y$, and the output velocity is picked up at $x_\mathrm{p} = 0.08L_x$, $y_\mathrm{p} = L_y$. The excitation signal consists of a single short pulse, as shown in the middle plot of Figure 6. During the simulation, the plate is gradually lifted upwards and back downwards (see top plot of Figure 6). Submersion into water is simulated using $a_\lambda = 32$ kg m^{-2} and and setting $\bar{p} = 1$ over the submerged region. The 'additional mass factor' is thus 2, which is in line with theoretical and experimental findings for the first bending mode [9]. The resulting variation of partial frequencies is clearly visible in the spectrogram shown in the bottom plot of Figure 6. Similar to the measured sound shown in Figure 2, the frequency variation differs considerably per partial, which is typical for this type of sound, and sonically distinguishable from phenomena in which all partial frequencies move synchronously.

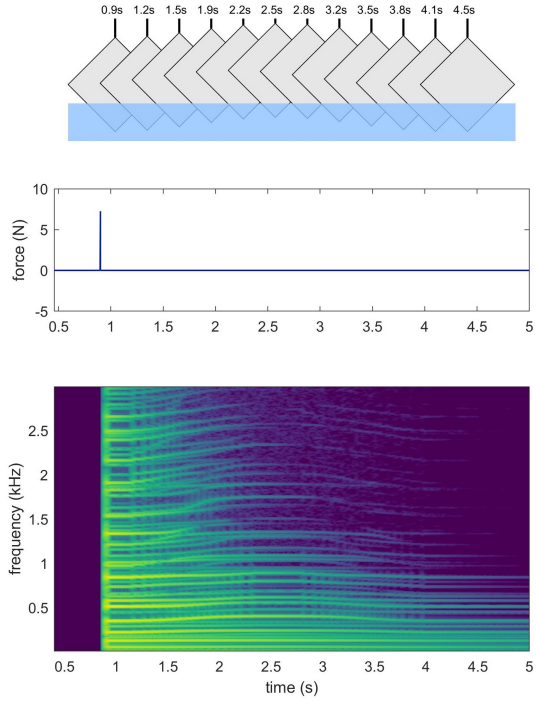

Figure 6. Water gong example. The top plot shows the height position of the suspended plate with respect to the water level. The middle plot shows the excitation signal and the bottom plot shows the output spectrogram.

5. TOWARDS A VIRTUAL-ACOUSTIC PLATE INSTRUMENT

This section outlines ideas and challenges the authors are currently encountering and addressing in applying the methodology towards developing a virtual-acoustic plate instrument.

5.1 Regional vs Global Contact

Recent publications [10, 11] discuss the development of a virtual-acoustic plate prototype instrument, the *Vodhrán*, featuring a modal synthesis algorithm for real-time simulation of plate vibrations, and utilising a Sensel Morph in combination with a contact microphone to sense tactile interaction. One of the ideas behind the design and development of the Vodhrán is achieving and controlling a degree of alignment with real-world counterparts in terms of sonically-relevant affordances.

With the Vodhrán, damping is effected via mapping the overall sum of non-percussive forces detected on the Sensel surface to the plate model's damping parameters. This provides intuitive damping control, but does not account for the specific damping region, and also lacks any additional effects (e.g. mass loading) that accompanies any real-world damping of plates. A real-time implementation of the proposed finite-difference model will allow a more natural, region-dependent form of damping.

One may use the same setup to facilitate and explore clamping configurations. Of particular interest is the potential to reconfigure the plate on the fly not through manipulations in software, but instead through actual clamping of the sensing device, as shown in Figure 7. This will open up ways of exploring the affordances of virtual-acoustic 'prepared plates' entirely through embodied interaction, leveraging skills and embodied knowledge acquired via interaction with real-world plates.

Figure 7. Clamping a Sensel Morph.

Contact that introduces mass-loading over a time-varying plate region, such as in the water gong example, could also be realised in real-time, but - if the affordances of the sensel are to be preserved - this will require an additional sensor interface. One strategy would be to employ a spring-loaded fader (similar to e.g. a synthesizer modulation wheel) to control the 'height' of the plate relative to the water level, as this would provide the musician with a haptic reference. This sensor would then drive the model's surface density via an additional term in the mapping, i.e. changing the first mapping in equation (6) to

$$\bar{\lambda} = a_\lambda \bar{p} + a_\mathrm{w} \bar{p}_\mathrm{w}, \tag{64}$$

where $\bar{p}_\mathrm{w}$ would be set to unity for the submerged region and zero elsewhere, and a_w is an appropriate scalar.

5.2 Computational Challenges

A number of challenges arise in the real-time implementation of the proposed model. Firstly, the implementation in finite-difference form will place limits on the possible size of the plate (in terms of the number of finite-difference nodes). Parallelisation techniques, such as Single Instruction, Multiple Data (SIMD) or Advanced Vector Extensions (AVX) have already proven useful in reducing the relevant CPU time [12, 13]. The new, additional challenges that emerge here are due to (a) the need to map the pressure data as sensed on the grid of the sensing device to the finite-difference grid, which involves 2-D (de-)interpolation, and (b) the need to carry out linear interpolation on the contact parameters, which are initially calculated at control rate (i.e. every N_b samples). One investigative route is to establish whether the grid mapping could be done on the sensing device, as such off-loading the main processor.

5.3 Model Extensions

While interesting sounds and articulations are possible with the proposed model, a few further extensions are of

interest. Firstly, most real-world (thin) plates are characterised by strong non-linear behaviour, and this plays an important role in many plates of musical interest. Such behaviour can be simulated by adding a non-linear term to the equation of motion, for example in the form of the von Kármán model [14]; finite-difference discretisations and associated energy analyses developed in [15, 16] could be readily applied to the current model, although with significant additional computational costs. The discretisation of the linear model could also be further investigated, in particular regarding ways to reduce numerical dispersion, possibly using parameterised schemes [17, 18]. Finally, many musical plates are circular, with a free edge; such a boundary could only be realised in the current approach using a staggered approximation of the curved edge. Possibly a better approach would be to apply finite-volume methods at the boundary, as for example employed in [19] for circular plates with fixed and clamped boundary conditions.

6. CONCLUSIONS

The proposed numerical model has been shown to enable simulation of specific, musically-relevant forms of non-excitational contact with a rectangular plate. An underlying motivation of the study is the exploration of new musical behaviours through simultaneous combinations of damping, clamping and mass-loading that would be impractical or expensive with mechanical technology. This will require real-time implementation of the proposed model in conjunction with design and development of sensing strategies, informed by wider instrument design notions. Further future work will focus on model extensions, including nonlinear plate modelling, and on application to membrane-based instruments, which mainly requires a simple replacement in the equation of motion of the stiffness term with a tension term. Of particular interest is the simulation of the tabla, as its performatory vocabulary consists of numerous intricate forms of dynamic contact [20]. Finally, the work presented is also relevant to non-musical sonic interactions, and is part of a wider project [3] that seeks to improve aural immersion in virtual and augmented reality settings.

Acknowledgments

This work was supported by the European Union's Horizon 2020 research and innovation programme under the Marie Skłodowska-Curie grant agreement No 812719. We thank the anonymous reviewers whose comments/suggestions helped improve and clarify this manuscript.

7. REFERENCES

[1] P. J. Gomez, "Modern guitar techniques; a view of history, convergence of musical traditions and contemporary works (a guide for composers and guitarists)," Ph.D. dissertation, UC San Diego, 2016.

[2] G. Crumb, "Echoes of Time and the River, Four Processionals for Orchestra (Echoes II)," Edition Peters, 1967.

[3] G. Cuzzucoli and V. Lombardo, "A physical model of the classical guitar, including the player's touch," *Computer Music Journal*, vol. 23, no. 2, pp. 52–69, 1999.

[4] F. Eckerholm and G. Evangelista, "The plucksynth touch string," in *11th Int. Conf. on Digital Audio Effects (DAFx-08)*, 2008.

[5] A. Bhanuprakash, M. van Walstijn, and P. Stapleton, "A finite difference model for articulated slide-string simulation," in *23rd International Conference on Digital Audio Effects (DAFx-20)*, vol. 1, 2020.

[6] S. Bilbao, *Numerical Sound Synthesis: Finite Difference Schemes and Simulation in Musical Acoustics*. Wiley Publishing, 2009.

[7] A. Torin, "Percussion instrument modelling in 3d: Sound synthesis through time domain numerical simulation," Ph.D. dissertation, University of Edinburgh, 2015.

[8] K. F. Graff, *Wave motion in elastic solids*, ser. Dover books on physics. New York, NY: Dover, 1991.

[9] M. Haddara and S. Cao, "A study of the dynamic response of submerged rectangular flat plates," *Marine Structures*, vol. 9, no. 10, pp. 913–933, 1996.

[10] L. Pardue, M. Ortiz, M. van Walstijn, P. Stapleton, and R. Matthews, "Vodhrán: collaborative design for evolving a physical model and interface into a proto-instrument," in *International Conference on New Interfaces for Musical Expression*, 2020, pp. 523–524.

[11] M. Rodger, P. Stapleton, M. V. Walstijn, M. Ortiz, and L. Pardue, "What makes a good musical instrument? a matter of processes, ecologies and specificities," in *Proceedings of the International Conference on New Interfaces for Musical Expression*, Birmingham, UK, 2020.

[12] C. Webb and S. Bilbao, "On the Limits of Real-Time Physical Modelling Synthesis with a Modular Environment," in *Proc. of the 18th Int. Conf. on Digital Audio Effects (DAFX-15)*, 2015.

[13] M. van Walstijn and S. Mehes, "An explorative string-bridge-plate model with tunable parameters," in *20th Int. Conf. on Digital Audio Effects (DAFx-17)*, 2017, pp. 291–298.

[14] R. Szilard, *Theory and Analysis of Plates: Classical and Numerical Methods*. Prentice-Hall, 1974.

[15] S. Bilbao, "A family of conservative finite difference schemes for the dynamical von karman plate equations," *Numerical Methods for Partial Differential Equations*, vol. 24, no. 1, pp. 193–216, 2008.

[16] M. Ducceschi, O. Cadot, C. Touzé, and S. Bilbao, "Dynamics of the wave turbulence spectrum in vibrating plates: A numerical investigation using a conservative finite difference scheme," *Physica D: Nonlinear Phenomena*, vol. 280-281, pp. 73 – 85, 2014.

[17] S. Bilbao, L. Savioja, and J. Smith, "Parameterized finite difference schemes for plates: Stability, the reduction of directional dispersion and frequency warping," *IEEE Trans. Audio, Speech, and Lang. Proc.*, vol. 15, no. 4, pp. 1488–1495", 2007.

[18] S. Orr and M. van Walstijn, "Modal representation of the resonant body within a finite difference framework for simulation of string instruments," in *12th Int. Conference on Digital Audio Effects (DAFx-09), Como, Italy*, 2009, pp. 213–220.

[19] B. Hamilton and A. Torin, "Finite difference schemes on hexagonal grids for thin linear plates with finite volume boundaries," in *DAFx*, 2014.

[20] A. Kapur, G. Essl, P. Davidson, and P. R. Cook, "The electronic tabla controller," *Journal of New Music Research*, vol. 32, no. 4, pp. 351–359, 2003.

[3] https://vrace-etn.eu/